

Overcoming Noise in Entanglement Distribution

Sebastian Ecker,^{1,2,*} Frédéric Bouchard,³ Lukas Bulla,^{1,2} Florian Brandt,^{1,2}
Oskar Kohout,^{1,2} Fabian Steinlechner,^{1,2,4,5} Robert Fickler,^{1,2,6,†} Mehul
Malik,^{1,2,7,‡} Yelena Guryanova,^{1,2,§} Rupert Ursin,^{1,2,¶} and Marcus Huber^{1,2,**}

¹*Institute for Quantum Optics and Quantum Information (IQOQI),
Austrian Academy of Sciences, Boltzmannngasse 3, 1090 Vienna, Austria.*

²*Vienna Center for Quantum Science and Technology (VCQ), Faculty of Physics,
University of Vienna, Boltzmannngasse 5, 1090 Vienna, Austria*

³*Department of physics, University of Ottawa, Advanced Research Complex, 25 Templeton, Ottawa ON Canada, K1N 6N5*

⁴*Fraunhofer Institute for Applied Optics and Precision Engineering IOF, Albert-Einstein-Strasse 7, 07745 Jena, Germany*

⁵*Abbe Center of Photonics - Friedrich-Schiller-University Jena, Albert-Einstein-Str. 6, 07745 Jena, Germany*

⁶*Photonics Laboratory, Physics Unit, Tampere University, Tampere, FI-33720, Finland*

⁷*Institute of Photonic and Quantum Sciences (IPaQS),
Heriot-Watt University, Edinburgh, Scotland, UK EH14 4AS*

Noise can be considered the natural enemy of quantum information. An often implied benefit of high-dimensional entanglement is its increased resilience to noise. However, manifesting this potential in an experimentally meaningful fashion is challenging and has never been done before. In infinite dimensional spaces, discretisation is inevitable and renders the effective dimension of quantum states a tunable parameter. Owing to advances in experimental techniques and theoretical tools, we demonstrate an increased resistance to noise by identifying two pathways to exploit high-dimensional entangled states. Our study is based on two separate experiments utilising canonical spatio-temporal properties of entangled photon pairs. Following these different pathways to noise resilience, we are able to certify entanglement in the photonic orbital-angular-momentum and energy-time degrees of freedom up to noise conditions corresponding to a noise fraction of 72 % and 92 % respectively. Our work paves the way towards practical quantum communication systems that are able to surpass current noise and distance limitations, while not compromising on potential device-independence.

I. INTRODUCTION

Quantum entanglement is one of the most peculiar and elusive properties of quantum systems, a key resource in quantum information processing [1] and an indispensable ingredient for device-independent quantum cryptography [2]. At the same time, entangled quantum systems are highly delicate since their entanglement is readily diminished by the slightest interaction with the environment. This is of particular relevance for the distribution of entangled photons over long distances outside of a protected laboratory environment, where particle loss and environmental noise are inevitable. Similar to classical communication, noise ultimately reduces the channel capacity and thus acts as a limiting factor for the link distance in quantum communications. Several proof-of-concept experiments have pushed the distribution distance of two-dimensional-entangled photon pairs over fiber [3–5] and free-space [6–8] links, while others have demonstrated the distribution of high-dimensional entangled quantum states [9–14].

Although it is not straightforward to certify high-dimensional entanglement from experimental data, its production in the process of spontaneous parametric down-conversion (SPDC) happens naturally. As a result of conservation laws in this process, the down-converted photon pairs are entangled in spatio-temporal properties such as energy-time [15–18], angle-angular momentum [19–22] and position-momentum [23–25].

At first glance, from an abstract information theoretic point of view, high-dimensional entanglement might seem to be essentially reproducible by just many copies of regular qubit entanglement. While there is actually a notable difference even in idealised pure states [26] and cryptographic settings [27], one of the main reasons for developing high-dimensional protocols has predominantly been the aforementioned free availability in down-conversion combined with the capability of storing more bits per communicated photon. Indeed, many such benefits of using high-dimensional encodings in quantum key distribution (QKD) have been investigated in the last decade [28–32], followed by experimental implementations in recent years [33–37]. Apart from an increased per-photon information capacity, an often implied advantage of employing high-dimensional entanglement is its potential for increased resistance to noise.

While it is indeed true that dimension-independent noise models show an increased resistance of entangled states to noise [38, 39], the actual advantages very much

* sebastian.ecker@oeaw.ac.at

† robert.fickler@tuni.fi

‡ m.malik@hw.ac.uk

§ yelena.guryanova@oeaw.ac.at

¶ rupert.ursin@oeaw.ac.at

** marcus.huber@univie.ac.at

depend on the physical implementation. Different high-dimensional degrees of freedom (DOFs) are bounded by different operational constraints. Thus, it has remained an open question whether practical improvements using high-dimensional entanglement can actually manifest its promised advantages.

In this letter, we expound potential pathways to an increased resilience to noise by utilising entanglement in high dimensions. We conduct two experiments, exploiting the most paradigmatic platforms for generating high-dimensional entangled quantum states, namely photons entangled in energy-time as well as transverse position-momentum. We show that for each high-dimensional encoding method and its associated state-of-the-art technology, there is an appropriate pathway to verify entanglement in conditions where qubit entanglement cannot be distributed due to extreme external noise levels. We are further able to characterise a realistic trade-off between dimensionality and robustness to find optimal and flexible encodings for both implementations and different background conditions, thereby revealing the transformative potential of high-dimensional quantum information.

II. PATHWAYS TO NOISE RESILIENCE

Almost all quantum experiments aim to harness a physical process that is expected to yield a pure entangled state. If the system is bipartite, and assuming that the experiment is ideal, then the entangled state can be represented in the Schmidt basis $|\psi_{AB}\rangle = \sum_i \lambda_i |ii\rangle$. Needless to say, experiments are seldom ideal, and a number of factors contribute to spoiling the state, during both its generation and its manipulation. Errors could, for example, be introduced during the distribution of the state via quantum channels or through imperfect measurement devices. Moreover, background photons inevitably introduce noise, resulting in a reduction of the signal-to-noise ratio at the read-out. It is well known that noise deteriorates entanglement and the extent to which entanglement persists despite the presence of noise is known as ‘noise resistance of entanglement’ [1]. The degree to which the initially pure state is degraded is often estimated using a white noise model, i.e. by mixing the target state $|\psi\rangle$ with the maximally mixed state:

$$\hat{\rho} = p |\psi\rangle \langle\psi| + \frac{1-p}{d^2} \mathbf{1}_{d^2}. \quad (1)$$

One may also note that this model captures particle loss for the maximally entangled state $|\psi\rangle = |\Phi^+\rangle := \frac{1}{\sqrt{d}} \sum_i |ii\rangle$, where with probability p the state remains intact, and with probability $1-p$ a particle from a pair is lost. The measurement statistics of the lost photon correspond to the maximally mixed state, while the statistics of the partner photon are replaced by the marginal. In the case of the maximally entangled state, this marginal is also maximally mixed $\text{Tr}_B |\Phi^+\rangle \langle\Phi^+| = \frac{1}{d} \mathbf{1}$, resulting in the model in (1). For this ‘isotropic’ state, the result-

ing tolerance to noise, i.e. the critical p_c after which the state becomes separable, scales as $p_c = \frac{1}{d+1}$. This can already be concluded from the first criteria for mixed state entanglement, such as positivity under partial transposition [40, 41] and has already been pointed out in early literature [42, 43]. While for general states such resistance to depolarizing noise is quite generic [44], physical modeling can reveal even further avenues of avoiding noise in high-dimensions [38]. We argue in Sec. III, that the noise introduced in both our experiments is close to white. Nonetheless, it is important to emphasise here, that we do not assume any noise model when analysing the experimental data for entanglement – the simple noise model only serves as a motivating example for why we should be expecting an increased noise resistance and it is not needed for performing or analysing the experiment. In a realistic experimental setting, loss can affect the measurement statistics in more complex ways, such as introducing accidental coincidence counts due to detector or background noise. A more quantitative analysis of the precise role of noise in photonic entanglement has been performed recently [38], and supports our experimental results by demonstrating a clear advantage of going to high dimensions. For more general states, bipartite depolarizing maps [44] capture different loss rates or detection efficiencies and can be solved analytically for any dimension. The common feature of these noise models is the fact that it is possible for the noise resistance to increase linearly with the system dimension d_S . As d_S grows, so does the so-called ‘dimensionality of entanglement’. Thus, one should, in principle, be able to overcome any amount of noise, and detect entanglement, simply by looking in systems of high-enough dimension. Despite this feature, there are several reasons why this idea has not yet manifested in any practical setups. First, certifying entanglement requires one to collect enough information about the underlying quantum state. The number of measurements required to do this scales *at least* linearly with the size of the system [45]. Second, the dimension of a system is not a fundamentally tunable parameter in an experiment and finally, the noise very much depends on the physical implementation of the chosen scheme. The theoretical description of spatio-temporal degrees of freedom of any photon state is infinite-dimensional,

$$|\psi\rangle_{\text{photon}} = \sum_s \int d\mu(x) \psi_s(x) |x, s\rangle \quad (2)$$

where s is the polarisation DOF, x the position and $\mu(x)$ a measure over the space. It then follows that the description of temporally or spatially entangled photon states is also infinite-dimensional. Despite this, any laboratory measurement still requires one to discretise these DOFs. The discretisation depends on the measuring device; for example, to discretise temporally entangled states one could time-resolve photon detections using high-precision clocks. For states entangled spa-

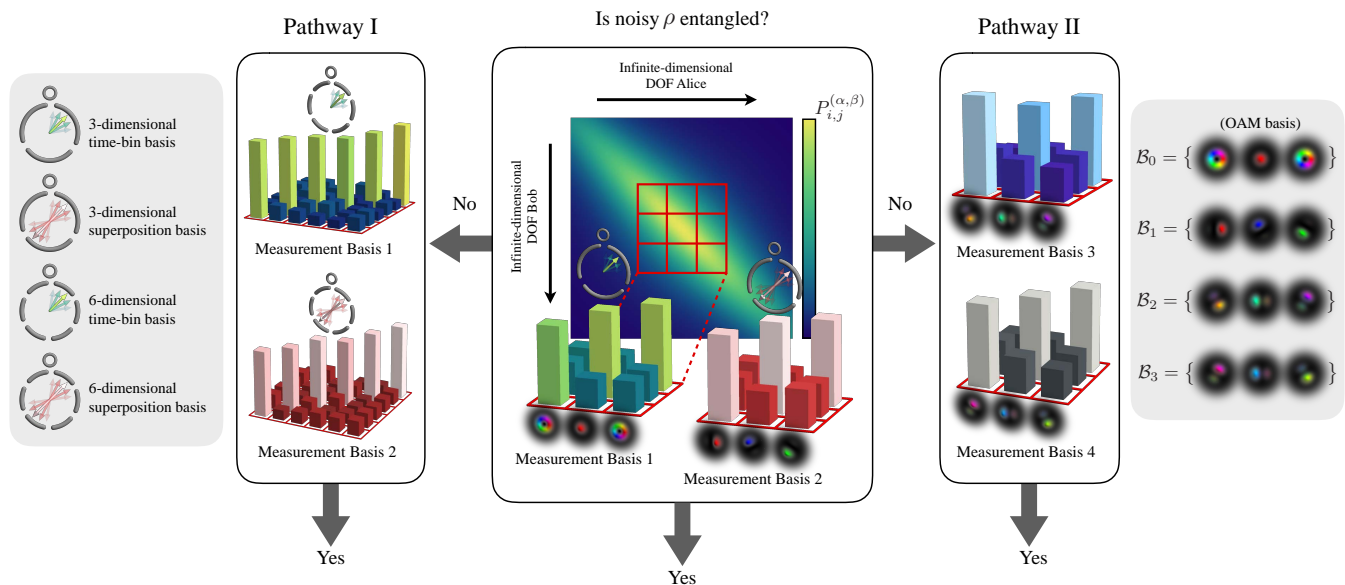


FIG. 1. Illustration of the pathways to noise resilience. A mixed entangled state ρ shared by Alice and Bob is encoded in spatio-temporal properties of photon pairs. Each of the infinite-dimensional degrees of freedom (DOF) of the photons can be discretised and measured in two bases (central panel). If both measurements are insufficient to certify entanglement in the noisy state, there are two pathways to recover it: Fine-graining to higher dimensions (Pathway I, left panel) and measuring in additional bases (Pathway II, right panel). In Pathway I, noise is ‘diluted’ by discretising the existing state space further, resulting in an increased signal-to-noise ratio. Pathway II exploits the existence of more than two mutually unbiased measurement bases in higher dimensions, providing additional information about the non-classicality of the state. The bar charts illustrate the joint probability $P_{i,j}^{(\alpha,\beta)}$ of measuring Alice’s modes i in the basis α and Bob’s modes j in the basis β .

tially, one could perform spatial mode measurements using spatial light modulators or cameras. All of these techniques have limited resolution; this means that by increasing the dimension of the states (i.e. discretising further) one will often encounter additional sources of noise, e.g. through cross-talk or additional measurement channels, which consequently lead to dimension-dependent noise factors $p(d)$ entering into the models. Thus, while high-dimensional entanglement presents an increased resistance to noise with increasing dimension on paper, it is not clear whether this theoretical advantage can be exploited in a real experiment.

Nevertheless, noise resistance of entanglement is a highly desirable feature in quantum communication and is of utmost importance for fundamental reasons. If one is able to demonstrate the persistence of entanglement, simply by discretising the description of systems, then one may be closer to understanding the fundamental limits on the information capacity of single photon quantum communication channels. In spite of this potential, not a single quantum experiment to date has been able to show an increase in noise resistance in a controlled fashion. In this work, we present two experiments that discretise continuous DOFs to encode information in high-dimensional quantum systems to explicitly demonstrate an increased resilience to environmental noise. These paradigms are illustrated in Fig. 1. It is to be read as a flow chart, starting in the center where a hypothetical noisy quan-

tum state ρ is tested for entanglement by making measurements in two bases. If none is found, one has two options, depending on the DOF and its technological constraints. The first pathway (Fig. 1 left) is to fine-grain or partition the quantum state to higher dimensions, for example by discretising an energy-time entangled state to a higher temporal resolution. Alternatively, one may explore pathway II (Fig. 1 right), which exploits the existence of more than two mutually unbiased bases (MUBs) in high dimensions. For example, measurements of an orbital-angular-momentum (OAM) entangled state can be made in additional bases, providing more information about the state. In both cases, entanglement can be recovered from a state in an assumption-free manner, where no entanglement could previously be certified through standard techniques.

III. EXPERIMENTAL IMPLEMENTATION

Here, we showcase two photonic experiments that demonstrate high-dimensional noise resilience of entanglement via the above-described two pathways. In the first experiment we follow pathway I and exploit energy-time entanglement, while in the second experiment we take pathway II to explore the orbital-angular-momentum DOF, both encodings that have seen rapid experimental progress in recent years [1]. The basic

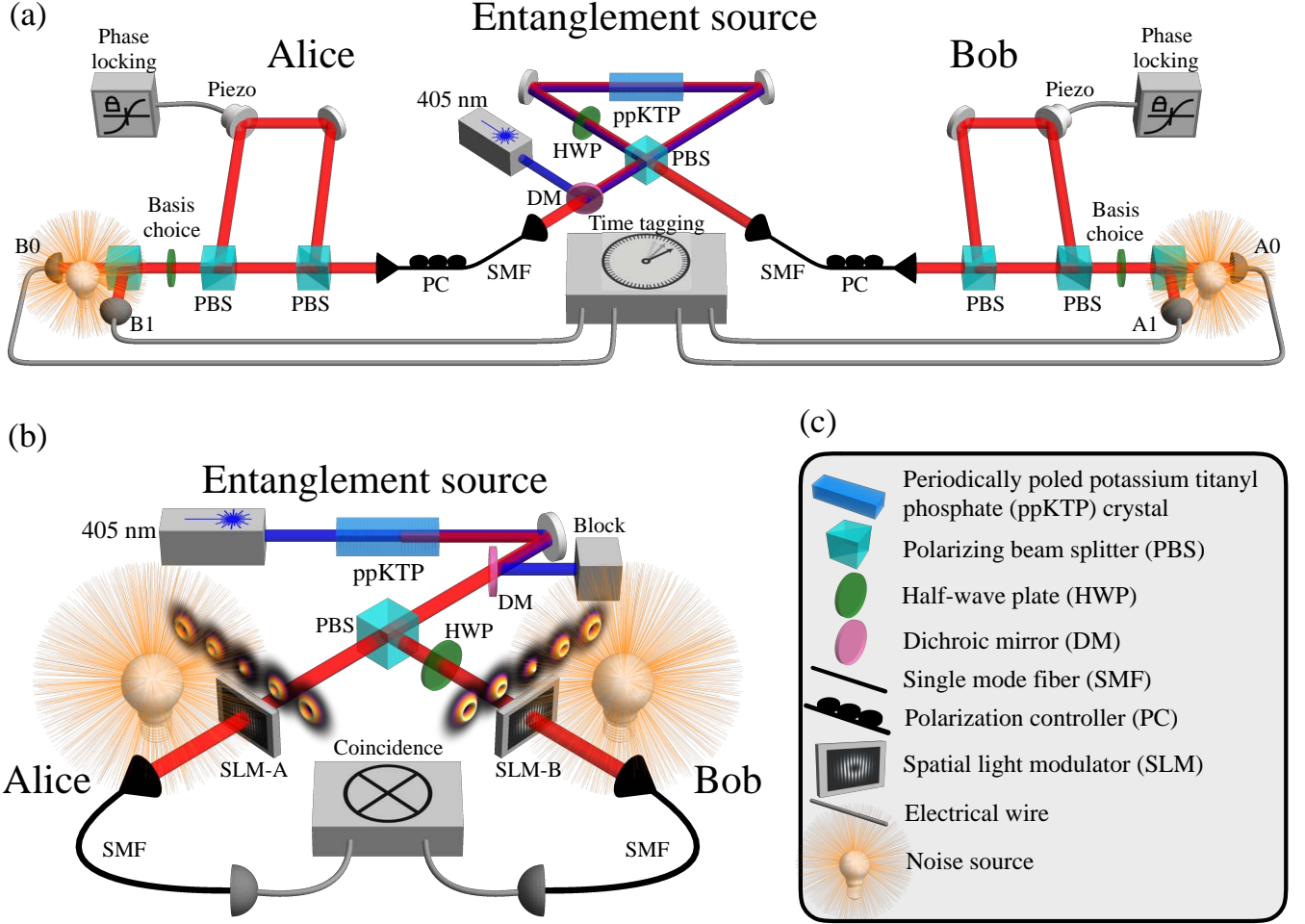


FIG. 2. Experimental setup for (a) energy-time and (b) orbital angular momentum (OAM) degrees of freedom. In both experiments, a 405 nm continuous-wave laser produces high-dimensionally entangled photon pairs in a ppKTP crystal exploiting type-II spontaneous parametric down-conversion (SPDC). The noise is optically added by intensity-adjustable light sources and single-photon detection is accomplished using avalanche photo diodes. (a) Additional polarization entanglement is generated by bidirectionally pumping the crystal in a polarization Sagnac interferometer. The polarization basis the photon pairs are measured in after an actively-stabilised post-selection-free Franson interferometer defines the measurement basis in the time domain. Each detection event is time-tagged and recorded by means of a time-to-amplitude converter. (b) The OAM-entangled pairs are split depending on their polarization, analysed through mode filtering by modulating the complex amplitude of the photons and subsequently coupled into SMFs. Coincidence counts are recorded using a coincidence logic.

premise of both experiments is to create photon pairs, and show, via a set of appropriately chosen measurements, that these pairs remain entangled even in the presence of high levels of noise. To generate the pairs in both experiments we appeal to spontaneous parametric downconversion (SPDC).

First, let us consider the creation of photon pairs entangled in energy-time. In the nonlinear SPDC process, a crystal pumped with photons of frequency ω_P will spontaneously produce a pair of photons with frequencies ω_0 and ω_1 . The total energy is strictly conserved such that, despite the crystal producing photon pairs with a finite bandwidth, the sum of their frequencies is constant: $\hbar\omega_P = \hbar\omega_0 + \hbar\omega_1$. This results in the emission of two photons that are highly entangled in energy. Since the

spectral linewidth and the coherence time are inversely related, a narrow pump bandwidth results in a long coherence time for possible photon pair emissions, giving rise to entanglement in the time-domain with Schmidt numbers up to $\sim 10^9$ under realistic experimental assumptions [33, 46]. In our scheme we utilize ancillary entanglement in the polarization DOF to facilitate interference in the time domain.

A similar narrative holds for the second experiment, which produces photons entangled in the orbital-angular-momentum (OAM) DOF. Here, the strict conservation of momentum in the SPDC process $\hbar l_p = \hbar l_0 + \hbar l_1$ results in the production of photon pairs anti-correlated in OAM $\hbar l_0 = -\hbar l_1$ for a Gaussian-mode pump photon with $\hbar l_p = 0$, leading to entanglement in the OAM-angular position

variables [21]. The (theoretically) infinite-dimensional states produced by the two experiments can be written as

$$|\Psi\rangle_{\text{ET-pol}} = \int dt f(t) |t\rangle_A |t\rangle_B \otimes |\phi^-\rangle_{AB} \quad (3)$$

$$|\Psi\rangle_{\text{OAM}} = \sum_{\ell=-\infty}^{\infty} c_{\ell} |-\ell\rangle_A |\ell\rangle_B, \quad (4)$$

where $f(t)$ is a continuous function of time, corresponding to the coherence profile of the laser; $|\phi^-\rangle_{AB} = \frac{1}{\sqrt{2}}(|H\rangle_A |H\rangle_B - |V\rangle_A |V\rangle_B)$ is a polarisation-entangled Bell state; $|\pm\ell\rangle$ is the state of a photon carrying an OAM quantum number of $\pm\ell$ and c_{ℓ} is a complex probability amplitude, which is defined by the spatial characteristics of the crystal and pump beam.

In order to gain meaningful insight into noise resilience, both states must be appropriately discretised. In the energy-time experiment, we measure the time of arrival of entangled photon pairs by discretising a time-frame of duration F into bins and recording which bin a photon is detected in. The duration of F is fixed and we divide it into an integer number of time-bin modes d , each corresponding to a duration t_d , i.e. $F/d = t_d$ (see Supplemental Material, Sec. 3 [47]). In pathway II, we choose a finite cut-off to the theoretically infinite sum over modes, such that the modes with OAM quantum numbers $l \in \{-D, \dots, D\}$ are spanning a $2D + 1$ - dimensional Hilbert space. Thus, ideally, the states generated by the experiments would be close to the forms

$$|\Psi\rangle_{\text{ET-pol}} = \sum_{j=1}^d \alpha_j |j\rangle_A |j\rangle_B \otimes |\phi^-\rangle_{AB} \quad (5)$$

$$|\Psi\rangle_{\text{OAM}} = \sum_{\ell=-D}^D c_{\ell} |-\ell\rangle_A |\ell\rangle_B, \quad (6)$$

where $|j\rangle$ refers to a photon in a discrete time-bin state whose duration is t_d for $j \in \{1, \dots, d\}$ and α_j is a complex probability amplitude.

Despite investigating different DOFs, the experiments have similar characteristic features, as shown in Fig. 2. In both schemes, a nonlinear crystal is pumped with a continuous-wave diode laser to generate photon pairs, which then pass through a setup consisting of measurement elements and an external noise source. In addition, the entanglement dimensionality for both cases (d for energy-time and $d = 2D + 1$ for OAM) is strongly dependent on the pump characteristics. In the energy-time experiment (Fig. 2(a)), a narrow-bandwidth pump ensures a large Schmidt number, while in the OAM experiment (Fig. 2(b)), a large pump mode with a well-defined transverse momentum results in high-dimensional OAM-entanglement. For additional experimental details, please see the Appendixes A and B. In both experiments, noise is introduced in the form of background photons generated by sources of light sim-

ulating a realistic operational environment for a quantum communication system. In the energy-time experiment, fine-adjustable light emitting diodes placed near the detectors introduce background counts—simulating a scenario where classical light may be co-propagating with a quantum signal. In the OAM experiment, background counts are introduced by increasing the intensity of the ambient light in the lab up to daylight conditions, which is a realistic scenario for free-space experiments using large aperture telescopes. White noise is generated in the energy-time experiment by employing two independent noise sources for Alice and Bob, thus eliminating temporal correlations, while in the OAM experiment white noise is introduced by placing the noise source after the spatial light modulators, ensuring mode-independent noise generation. In both cases, we quantify the amount of noise introduced via the noise fraction NF , which corresponds to the fraction of counts in our data that arise from noise. Intuitively, $NF = \frac{\#\text{noise counts}}{\#\text{total counts}}$, which takes on values from 0 (no noise) to 1 (complete noise). A more rigorous definition of the noise fraction NF and its computation from experimental data is presented in the Supplemental Material, Sec. 2 [47].

IV. ENERGY-TIME ENTANGLEMENT (PATHWAY I)

The first pathway to noise-resilience is implemented by fine-graining measurements of the photon arrival time. As outlined, we discretise a time-frame into d time-bins and record the bin that a photon is detected in. The goal of the experiment is simple: by increasing the dimension d of the state in Eq. (5) through fine-graining, we want to certify entanglement of noisy quantum states, which is otherwise concealed by noise.

To this end, we collect statistics about the state in two bases. The first measurement is in the same basis as the state in Eq. (5). Projecting onto the time-bin states $|i, j\rangle$, with $i, j \in \{1, \dots, d\}$, is accomplished by recording the time of arrival of single photons with a detector and a precise clock, which constitutes a multi-outcome measurement. The second measurement is more difficult as it must be performed in a superposition basis of the time-bin states. This can be achieved by delaying the state $|i\rangle$ for a duration corresponding to f time-bins and subsequently interfering it with the state $|i + f\rangle$. We realize this in our experiment by utilising a Franson interferometer [48], which employs an unbalanced interferometer for Alice and Bob respectively (see Fig. 2(a)). The long interferometer arm delays the state $|i\rangle$ relative to the state $|i + f\rangle$, which occupies the spatial path of the short interferometer arm. The second basis therefore projects onto the states $\frac{1}{\sqrt{2}}(|i, j\rangle + e^{i\phi}|i + f, j + f\rangle)$, where the phase ϕ is set by the sum of the two individual interferometer phases and $i, j \in \{1, \dots, d\}$. However, without active switching, this interferometer will also project onto the states $|i, i + f\rangle$ and $|i + f, i\rangle$, which are not interfering

and thus must be discarded in coincidence post-selection. Since we investigate high-dimensional states, these non-interfering events are part of our state space and we may not simply discard them. We tackle this problem by employing a postselection-free Franson interferometer [49]. In this scheme, polarization-entanglement is exploited to deterministically route the photon pairs in the Franson interferometer. This requires a hyperentangled source state [50, 51] in polarization and energy-time. We generate the additional polarization entanglement by bidirectionally pumping a nonlinear crystal centered in a polarization Sagnac interferometer [52, 53], which enables us to use the polarization DOF to switch between the two measurement basis in the time domain (see Appendix A for details). Our entanglement certification is based on a dimension-dependent entanglement witness $W(\rho_{ET}, d)$, where, from Eq. (5) $\rho_{ET} = \text{Tr}_{\text{pol}} |\Psi\rangle\langle\Psi|$. The relation from the count statistics of the two measurements to the state ρ_{ET} is rather involved and can be found in the Supplemental Material, Sec. 1 [47]. Here, it suffices to say that our state is entangled if $W(\rho_{ET}, d) > 0$.

We introduce increasing levels of external noise corresponding to a noise fraction NF ranging from 0 to near-unity, in order to transition from a close-to-pure to a mixed state. Following Pathway I, we now fine-grain our state space to higher dimensions. The frame duration F is fixed at 320 clock cycles and we discretise the frame in four ways according to $F/d = t_d$ for $d \in \{10, 20, 40, 80\}$. This choice of dimensions depend on the imbalance of the Franson interferometer, and is detailed in Appendix A. Figure 3(a) illustrates the scaling of the entanglement witness W for different dimensions as the noise fraction NF is increased. This increase is accomplished by incrementing the amount of external optical noise, with the sequence of data points in each dimension corresponding to the same external noise levels. The noise threshold, which is the maximal NF for which entanglement can be certified, increases with higher dimensions, indicating noise resilience (see inset). For $d = 10, 20, 40, 80$ the noise thresholds steadily increase from 0.57, 0.76, 0.86 to 0.93, respectively. As a consequence of fine-graining, the crosstalk between time-bins increases due to fundamental and technical limitations. This excess noise becomes relevant once the time-bin size is smaller than the timing resolution of the detectors, as is the case with $d = 40$ and $d = 80$. For these discretizations, the NF is significantly increased even in the absence of external noise, indicated by the first data points in each dimension. Fine-graining at low external noise levels also reduces the witness violation, while for noise levels close to the noise threshold, fine-graining results in the recurrence of otherwise obscured entanglement.

V. ORBITAL ANGULAR MOMENTUM ENTANGLEMENT (PATHWAY II)

The second pathway to noise resilience takes advantage of the larger number of mutually unbiased bases in higher dimensions. Here, we explore this pathway using measurements of orbital angular momentum MUBs, for which precise measurements techniques have only recently been developed [54]. Mutually unbiased bases are an invaluable tool in many quantum information tasks, such as quantum state tomography, quantum cryptography, and entanglement certification. They consist of a set of orthonormal bases $\{\mathcal{B}_\alpha\}$, where $\mathcal{B}_\alpha = \{|\psi_m^{(\alpha)}\rangle\}$, $m \in \{0, 1, \dots, d-1\}$ and $\alpha \in \{0, 1, \dots, d\}$. Such a set is called mutually unbiased if and only if,

$$\left| \langle \psi_m^{(\alpha)} | \psi_n^{(\beta)} \rangle \right|^2 = \delta_{\alpha\beta} \delta_{mn} + (1 - \delta_{\alpha\beta})/d, \quad (7)$$

where $\delta_{i,j}$ is the Kronecker delta. In dimensions that are powers of prime numbers, it is known that there exists exactly $(d+1)$ MUBs. Surprisingly, for dimensions that are not powers of prime numbers, finding the number of MUBs and their elements remains an open problem [55]. For the case of prime dimensions and $\alpha \geq 1$, a MUB element is explicitly given by $|\psi_m^{(\alpha)}\rangle = (1/\sqrt{d}) \sum_{j=0}^{d-1} (\omega_d^m)^{d-j} (\omega_d^{-(\alpha-1)})^{s_j} |j\rangle$, where $\omega_d = \exp(2\pi i/d)$ and $s_j = j + \dots + (d-1)$. In the current experiment, we use the intensity flattening technique [54] to measure the correlations of the photon pairs in all MUBs (see Appendix B for further details). The joint probability of Alice and Bob measuring states $|\psi_m^{(\alpha)}\rangle$ and $|\psi_n^{(\beta)}\rangle$ respectively, is given by $P^{(\alpha,\beta)}(m,n)$. For a complete set of joint measurements by Alice and Bob in bases \mathcal{B}_α and \mathcal{B}_β respectively, we define the correlation visibility as $V^{(\alpha,\beta)} = \sum_{i=0}^{d-1} P^{(\alpha,\beta)}(i,i)$. Following the analysis of [56], we obtain an upper bound for separable states by considering the sum of the visibilities over k MUBs, i.e. $\sum_j^{k-1} V^{(j,j)} \leq 1 + \frac{k-1}{d}$. In particular, for measurements in all $k = (d+1)$ MUBs, entanglement certification is achieved for $\sum_j^{k-1} V^{(j,j)} > 2$. Hence, in contrast to the case of energy-time entanglement described before, where detections are limited to measurements in two-dimensional subspaces but dimensions of up to 80, we are now able to fully characterize the generated states by performing high-dimensional projective measurements but we are limited to lower overall dimensions. However, this might be largely increased by using custom-tailored phase-matching [57] or by considering the complete space of transverse spatial modes, namely radial modes along with azimuthal modes.

As a starting point, we consider bi-dimensionally entangled OAM states of the form $(|1, -1\rangle + |-1, 1\rangle)/\sqrt{2}$. Entanglement is certified by measuring correlations in all three MUBs in the two-dimensional space of OAM

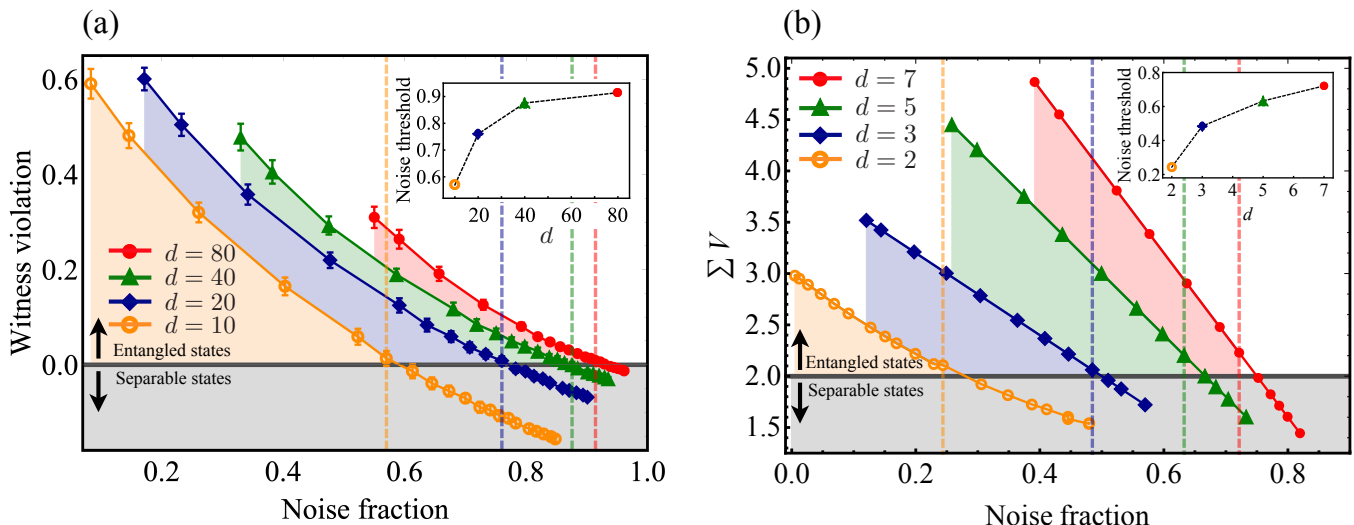


FIG. 3. Main results of our experimental demonstration of noise resistance for (a) energy-time entanglement and (b) OAM entanglement. Each plot depicts the violation strength of a suitably chosen entanglement witness against the noise fraction, i.e. the fraction of coincidence detections attributable to noise. In plot (a) the principal competition in achieving noise resistance is clearly visible. As the dimensionality is increased through fine-graining (Pathway I), more noise is induced (and thus the curves move to the right), while a higher noise resilience is achieved (thus the noise threshold also moves to the right). Plot (b) is qualitatively different, as it explores Pathway II. Instead of fine-graining, more modes are included in the analysis which allow for an increased number of mutual unbiased bases to be measured and thus also show a higher noise threshold with increasing dimension. The error bars correspond to 3 standard deviations of the mean, calculated by propagating the Poissonian error in the photon-counting rates via a Monte Carlo simulation, see Supplemental Material, Sec. 4 [47]. In (b), the error bars are smaller than the data points.

$|\ell = \pm 1\rangle$. Environmental noise is steadily added by gradually increasing the intensity of the ambient light present in the lab, corresponding to a noise fraction NF ranging from 0 to 0.8. Figure 3(b) shows how the sum of visibilities ($\sum V$) in $d + 1$ MUBs varies as a function of increasing noise fraction. Entanglement is always certified if $\sum V > 2$, irrespective of dimension. For $d = 2$, entanglement is certified for noise fractions up to 0.24. However, with increasing dimension, we are able to tolerate a higher noise fraction threshold, beyond which no entanglement can be certified (see inset). For $d = 3, 5$, and 7 , the noise fraction thresholds are 0.48, 0.63, and 0.72 respectively. The inset also shows that the noise threshold seems to be saturating as the dimension is increased. This is primarily due to the reduced fidelity of measurements in high dimensions, as well as our state moving further away from an ideal maximally entangled state as the dimension is increased. However, it is clear from our results that by increasing the state dimension, which in turn enables measurements in more bases, one can increase the resilience of entanglement to background noise. It is interesting to note that this could motivate the search for high-dimensional MUBs for any dimension, as communication systems should ideally be able to optimally operate beyond prime-dimensions.

VI. DISCUSSION

Our experimental results showcase the challenges and potential of overcoming noise through high-dimensional entanglement in quantum communication. While the necessary spatio-temporal entanglement is routinely generated in down-conversion, the real challenge is to encode information in these high-dimensionally entangled states. In other words, high-dimensional entanglement is already present in the workhorses of quantum communication, but routinely lost through coarse-graining and ignorance of modes. While this can be beneficial in removing noise from the signals, we observe a competition between two key factors: High-dimensional encoding increases the noise resistance as the dimension grows through the two pathways we identified, but also adds additional noise with increasing dimension. This is a competition that will ultimately always be won by noise, otherwise single photons could carry an infinite amount of information. The ultimate goal is finding the sweet spot, where the increased noise resistance still trumps the additional noise and thus realises a practical improvement in noisy entanglement distribution. What we show in our two experiments is that this sweet spot is actually beyond dimension two and thus defies conventional wisdom in the field, calling for the development of high-dimensional protocols across photonic platforms. While we have used two different experiments to illustrate the two pathways

to noise resistance separately, both pathways could in principle be realised simultaneously in the same experiment. If one had access to multiple MUB measurements in time-bins or multi-outcome measurements in the spatial domain, one could harness both pathways, leading to an increase in measurable dimensionality and as a consequence, higher noise thresholds.

Our method of adding external noise, namely by fixing a constant luminosity light source close to our detectors, is a fairly realistic model of noise that captures the decreased signal-to-noise ratio in long-distance quantum communication, where detector dark counts start dominating the distance-attenuated single-photon pairs. On the other hand, our experiments also simulate daylight conditions for free-space quantum communication [58, 59], where background photons will trigger accidents in the very same way as our artificial lamps do. In both of these scenarios, the most detrimental noise in the quantum channel is white, which motivated us to employ noise sources of this characteristic in our experiments.

The most remarkable outcome of this study is the fact that we demonstrate the possibility to certify entanglement that was otherwise obscured. In other words, entanglement really was able to overcome physical noise in the implementation and reveal itself by going to higher dimensional encodings. We would like to note that this is not only a proof-of-principle implementation, but it is ready to be also directly adopted for long distance or free-space quantum communication [9, 60]. At least for the energy-time experiment we could use the exact same setup, whereas for the OAM experiment we would require a multi-outcome measurement, such as the recently developed spatial mode sorter [61]. With the current single-outcome measurements, every element/dimension we add will experience the same environmental noise [since it directly couples to the single-mode fiber (SMF)], thus unfavourably influencing the competition between noise and entanglement, with the total noise fraction increasing at the same rate as the additional noise robustness. The noise fraction we measured nonetheless proves that, if one had a measurement technique where the noise distributes over multiple channels, we would have a tremendously increased resistance to physical noise outside of laboratory settings.

The obvious next challenge is the development of quantum communication protocols that make direct use of high-dimensional encodings. The fact that entanglement can be certified under extremely noisy background conditions motivates the question of whether such noisy entanglement can indeed be used to certify security of QKD or aid in other quantum information tasks. It has recently been proven that every entangled state, no matter how noisy, provides an advantage in entanglement-assisted classical communication [62]. In addition, every noisy entangled state also provides an advantage for the task of channel discrimination [63]. We hope that this study spurs further investigation into information theoretic protocols based on high-dimensional and noisy en-

tangled states, which can be distributed in regimes where no qubit communication is possible.

ACKNOWLEDGEMENTS

We thank Jessica Bavaresco for helpful discussions on OAM entanglement certification and data analysis. F.Brandt, M.H., M.M., R.F. and Y.G. acknowledge funding from the Austrian Science Fund (FWF): Y879-N27, I3053-N27, P31339-N27. M.M. acknowledges support from the QuantERA ERA-NET co-fund (Austrian Science Fund (FWF): I3773-N36) and from the UK Engineering and Physical Sciences Research Council (EPSRC) (EP/P024114/1). F.Bouchard acknowledges the support of the Vanier Canada Graduate Scholarships Program and the Natural Sciences and Engineering Research Council of Canada (NSERC). R.F. acknowledges the support of the Academy of Finland (Competitive Funding to Strengthen University Research Profiles - decision 301820 and Photonics Research and Innovation Flagship - decision 320165). We acknowledge funding from the Austrian Research Promotion Agency (FFG) Quantenforschung und -technologie (QFTE) Contract 870003, Austrian Science and Applications Programme (ASAP) Contract 854022 and Contract 866025 and ESA European Space Agency Contract 4000112591/14/NL/US.

S.E. and F.Bouchard contributed equally to this work; M.M., R.U. and M.H. conceived the project; S.E., L.B. and O.K. designed and developed the energy-time entanglement experiment under the guidance of F.S. and R.U.; F.Bouchard and F.Brandt designed and developed the orbital-angular-momentum entanglement experiment under the guidance of R.F., M.M. and M.H.; M.H. and Y.G. established the entanglement certification methods; S.E., F.Bouchard, R.F., M.M., Y.G. and M.H. wrote the first draft of the manuscript; All authors discussed the results and reviewed the manuscript; M.H. supervised the whole project.

APPENDIX A: ENERGY-TIME ENTANGLEMENT EXPERIMENT

The experimental setup can be divided into a hyperentangled photon pair source, a Franson interferometer consisting of two imbalanced polarizing Mach-Zehnder interferometers (PMZI) and a detection- and time tagging-unit. Our source is based on SPDC in a 20 mm-long periodically poled potassium titanyl phosphate (ppKTP) crystal designed for type-II quasi-phase-matching. A grating-stabilized photodiode (Toptica DL pro) emitting at a wavelength of 405 nm is generating the pump field for the SPDC. Due to a narrow pump bandwidth of $\Delta\nu_{\text{FWHM}} \sim 500$ kHz, the down-converted signal and idler fields are energy-time-entangled within a coherence time of $t_{\text{coh}} = 1/(\pi\Delta\nu_{\text{FWHM}}) \sim 636$ ns.

The ppKTP crystal is temperature-tuned to produce wavelength-degenerate photon pairs at 810 nm. In order to obtain polarization entanglement, the crystal is bidirectionally pumped in the center of a polarization Sagnac interferometer [52, 53]. After 3-nm bandpass filtering and single-mode coupling, we detect an entangled photon pair rate of 15 kcps per mW of pump power with a heralding efficiency of 20% in both signal and idler modes.

The single photons are then guided to two bulk optics PMZIs with an imbalance between long and short interferometer arm of 2.67 ns. The imbalance of the two PMZIs is matched up to the correlation length of the photon pairs ($\sim 800 \mu\text{m}$). By adjusting the phases $\phi_{A/B}$ of Alice's/Bob's PMZI, we see Franson interference with a phase of $\phi_{\text{Franson}} = \phi_A + \phi_B$. All of our measurements in the superposition or Franson basis are performed at maximal Franson interference contrast ($\phi_{\text{Franson}} = 0$ or π), which requires phase-stability of the PMZIs over the measurement time. Active phase stabilisation of both PMZIs is achieved by a control loop of a Piezo actuator displacing an interferometer mirror and the difference signal from two photodiodes indicating the interference contrast. This interference signal is provided by a 780.241-nm stabilisation laser (Toptica DL Pro) propagating in the same spatial interferometer mode as the single photons. It is injected into the PMZIs via the unused port of the first polarizing beam splitter (PBS) and measured at the output of the unused port of the second PBS, where the polarisation contrast is measured by fast photodiodes (Thorlabs - DET 10 A/M) in a polarisation basis conjugate to the polarisation basis defined by the PMZIs. The stabilisation laser is frequency-locked to a hyperfine transition of ^{85}Rb , obtained by saturated absorption spectroscopy, resulting in a wavelength stability of $\sim 0.6 \text{ fm/min}$.

We choose the measurement basis in the energy-time domain by changing the polarization measurement basis after the PMZI, effectively switching the interferometer on or off by erasing or revealing the interferometer path information. Performing a polarization measurement in the PMZI-defined rectilinear basis corresponds to a measurement in the computational basis, while projecting the photons in a mutually unbiased polarization basis corresponds to a measurement in the Franson basis (see Supplemental Material, Sec. 3 [47] for a stringent formal treatment). Noise is optically added to the measurement data by means of fine-adjustable light emitting diodes (LEDs) powered by a battery, ensuring time-invariant noise generation. We detect both polarization components on Alice's (detectors A0 and A1) and Bob's (detectors B0 and B1) side by means of multimode-coupled single-photon avalanche diodes (Excelitas SPCM-800-11) with a measured FWHM timing jitter of $< 800 \text{ ps}$ between two detectors. The detection events are time-tagged employing a time to amplitude converter (AIT TTM8000) with a clock resolution of 82.3 ps.

Post-processing of the time-tagged data is realized

by binning the detection events of each channel into dimension-dependent time-bins of duration $t_d = F/d$, where F is the duration of one frame. Since the imbalance of our interferometers is fixed and corresponds to 32 clock cycles, only time-bin durations which obey $f \cdot t_d = 32$ clock cycles give rise to well-defined Franson interference $|i, i\rangle + e^{i\phi_{\text{Franson}}} |i + f, i + f\rangle$, where f is an integer corresponding to the time-bin shift. To this end, in order to see interference, we investigate dimensions which satisfy $d = \frac{f \cdot F}{32}$ for integer f and d . For our setup parameters and for a time-frame duration of $F = 320$ clock cycles this corresponds to $d \in \{10, 20, 40, 80\}$.

The discretizations to different dimensions are performed on the same set of measurement data. Since we are tracking photons emitted from a photon pair source, our state space is intrinsically bipartite, and only those time-frames which contain exactly one detection event on Alice's side and exactly one on Bob's side are kept; all others are discarded (e.g. no detection event in Alice's and 1 detection event in Bob's detectors per frame). The detection events which are kept are then sorted into count matrices pertaining to the detectors that clicked (A0-B0, A1-B1, A0-B1, A1-B0). These 4 matrices in both measurement bases are used to reconstruct the part of the state ρ_{ET} required in the subsequent entanglement certification.

Since the timing-jitter of the detectors is one order of magnitude greater than the clock resolution of the timetagger, our overall timing resolution is dominated by the detector jitter. Therefore, crosstalk errors between time-bins will sharply increase once the time-bin duration t_d is on the order of the timing-jitter of the detector, which is the case for $t_d = 8$ clock cycles = 658.4 ns.

The witness used to certify entanglement was derived using the entropy vector formalism in [64]. For each dimension d , the underlying state ρ_{ET} is not separable (i.e. entanglement is certified) if $W(\rho_{\text{ET}}, d) > 0$, where

$$W(\rho_{\text{ET}}, d) := \sum_i^{d-f} |\langle ii | \rho_{\text{ET}} | i + f, i + f \rangle| - \sqrt{\langle i, i + f | \rho_{\text{ET}} | i, i + f \rangle \langle i + f, i | \rho_{\text{ET}} | i + f, i \rangle}. \quad (\text{A1})$$

In order to compute the witness, one must reconstruct the underlying density matrix elements of ρ_{ET} from the experimental count matrices. These also depend on the polarisation degree of freedom, due to the use of a postselection-free Franson interferometer. Details of how to compute the witness from the count matrices produced by the experiment can be found in the Supplemental Material, Sec. 1 [47].

APPENDIX B: OAM ENTANGLEMENT - EXPERIMENT

We generate pairs of photons entangled in the orbital-angular-momentum (OAM) degree of freedom by pump-

ing a 5 mm long ppKTP crystal quasi-phase matched for type II SPDC. We use a 405 nm diode laser (Toptica iBeam Smart 405 HP) that is coupled to a single-mode optical fiber to ensure the best possible transverse coherence and mode profile, which is essential to obtain high-dimensionally entangled pairs of photons. The UV beam is focused by a 500 mm lens to a spot size of $430 \mu\text{m}$ ($1/e^2$ beam diameter) at the ppKTP crystal. We similarly temperature tune this crystal to produce pairs of wavelength-degenerate, orthogonally polarized photons at 810 nm. The photon pairs are recollimated by a 300 mm lens. This time the polarization DOF of the photons is solely used to deterministically split the photons at a polarization beam splitter, such that their spatial mode can be measured independently of each other. The photons are then made incident on phase-only spatial light modulators (Holoeye PLUTO), where a combination of computer-generated holograms and single-mode fibers (SMFs) are used to perform a generalized projective measurement in the OAM state space. Finally, the photons are detected by avalanche photodiodes and coincidence measurements are recorded within a coincidence time window of 5 ns using a custom-built logic. In the computational basis, measurements of photonic OAM may be accomplished by displaying a hologram generating the opposite OAM value, thus resulting in an outgoing beam with a flat

wavefront with an OAM value of $\ell = 0$ that will couple efficiently to the SMF using a 10-X microscope objective. This technique is also known as phase-flattening and has been widely used to measure the OAM content of an unknown beam [65]. However, in order to certify entanglement, it is necessary to perform measurements in additional bases besides the computational (OAM) basis, which leads to more complex mode structures (see Supplemental Material, Sec. 5 [47]). Thus, a more elaborate measurement scheme is required to accurately measure the general OAM state of the experimentally generated entangled pairs. We use a recently introduced technique called intensity flattening [54], that allows one to measure any arbitrary transverse spatial mode of light, including modes in any mutually unbiased basis of OAM. Although lossy, this technique yields extremely high detection fidelities. Using this source, after taking into account the lossy intensity masking holograms implemented at the spatial light modulators, we achieve coincidence count rates of 500 Hz in the fundamental Gaussian mode, 1000 Hz in the first-order OAM modes ($\ell = \pm 1$), 700 Hz in the second-order OAM modes ($\ell = \pm 2$), and 400 Hz in the third-order OAM modes ($\ell = \pm 3$). The associated singles count rates are given by 13 kHz, 20 kHz, 15 kHz, and 11 kHz.

-
- [1] Nicolai Friis, Giuseppe Vitagliano, Mehul Malik, and Marcus Huber, “Entanglement certification from theory to experiment,” *Nature Reviews Physics* **1**, 72–87 (2019).
- [2] Antonio Acín, Nicolas Brunner, Nicolas Gisin, Serge Massar, Stefano Pironio, and Valerio Scarani, “Device-Independent Security of Quantum Cryptography against Collective Attacks,” *Phys. Rev. Lett.* **98**, 230501 (2007).
- [3] Daniel Salart, Augustin Baas, Cyril Branciard, Nicolas Gisin, and Hugo Zbinden, “Testing the speed of ‘spooky action at a distance’,” *Nature* **454**, 861–864 (2008).
- [4] Takahiro Inagaki, Nobuyuki Matsuda, Osamu Tadanaga, Masaki Asoke, and Hiroki Takesue, “Entanglement distribution over 300 km of fiber,” *Opt. Express* **21**, 23241–23249 (2013).
- [5] Sören Wengerowsky, Siddarth Koduru Joshi, Fabian Steinlechner, Julien R. Zichi, Sergiy. M. Dobrovolskiy, René van der Molen, Johannes W. N. Los, Val Zwiller, Marijn A. M. Versteegh, Alberto Mura, Davide Calonico, Massimo Inguscio, Hannes Hübel, Liu Bo, Thomas Scheidl, Anton Zeilinger, André Xuereb, and Rupert Ursin, “Entanglement distribution over a 96-km-long submarine optical fiber,” *Proceedings of the National Academy of Sciences* **116**, 6684–6688 (2019).
- [6] Thomas Scheidl, Rupert Ursin, Alessandro Fedrizzi, Sven Ramelow, Xiao-Song Ma, Thomas Herbst, Robert Prevedel, Lothar Ratschbacher, Johannes Kofler, Thomas Jennewein, and Anton Zeilinger, “Feasibility of 300 km quantum key distribution with entangled states,” *New Journal of Physics* **11**, 085002 (2009).
- [7] Mario Krenn, Johannes Handsteiner, Matthias Fink, Robert Fickler, and Anton Zeilinger, “Twisted photon entanglement through turbulent air across vienna,” *Proceedings of the National Academy of Sciences* **112**, 14197–14201 (2015).
- [8] Juan Yin, Yuan Cao, Yu-Huai Li, Sheng-Kai Liao, Liang Zhang, Ji-Gang Ren, Wen-Qi Cai, Wei-Yue Liu, Bo Li, Hui Dai, Guang-Bing Li, Qi-Ming Lu, Yun-Hong Gong, Yu Xu, Shuang-Lin Li, Feng-Zhi Li, Ya-Yun Yin, Zi-Qing Jiang, Ming Li, Jian-Jun Jia, Ge Ren, Dong He, Yi-Lin Zhou, Xiao-Xiang Zhang, Na Wang, Xiang Chang, Zhen-Cai Zhu, Nai-Le Liu, Yu-Ao Chen, Chao-Yang Lu, Rong Shu, Cheng-Zhi Peng, Jian-Yu Wang, and Jian-Wei Pan, “Satellite-based entanglement distribution over 1200 kilometers,” *Science* **356**, 1140–1144 (2017).
- [9] Fabian Steinlechner, Sebastian Ecker, Matthias Fink, Bo Liu, Jessica Bavaresco, Marcus Huber, Thomas Scheidl, and Rupert Ursin, “Distribution of high-dimensional entanglement via an intra-city free-space link,” *Nature Communications* **8**, 15971 (2017).
- [10] Takuya Ikuta and Hiroki Takesue, “Four-dimensional entanglement distribution over 100 km,” *Scientific Reports* **8**, 817 (2018).
- [11] Daniele Cozzolino, Davide Bacco, Beatrice Da Lio, Kasper Ingerslev, Yunhong Ding, Kjeld Dalgaard, Poul Kristensen, Michael Galili, Karsten Rottwitz, Siddharth Ramachandran, and Leif Katsuo Oxenløwe, “Orbital angular momentum states enabling fiber-based high-dimensional quantum communication,” *Phys. Rev. Applied* **11**, 064058 (2019).
- [12] Jun Liu, Isaac Nape, Qianke Wang, Adam Valles, Jian Wang, and Andrew Forbes, “Multi-dimensional entanglement transport through single-mode fibre,” (2019),

- arXiv:1904.03114 [quant-ph].
- [13] Daniele Cozzolino, Emanuele Polino, Mauro Valeri, Gonzalo Carvacho, Davide Bacco, Nicolò Spagnolo, Leif K. K. Oxenløwe, and Fabio Sciarrino, “Air-core fiber distribution of hybrid vector vortex-polarization entangled states,” *Advanced Photonics* **1**, 1 – 9 (2019).
 - [14] Huan Cao, She-Cheng Gao, Chao Zhang, Jian Wang, De-Yong He, Bi-Heng Liu, Zheng-Wei Zhou, Guo-Xuan Zhu, Yu-Jie Chen, Zhao-Hui Li, Si-Yuan Yu, Yun-Feng Huang, Chuan-Feng Li, and Guang-Can Guo, “Distribution of high-dimensional orbital angular momentum entanglement at telecom wavelength over 1km oam fiber,” (2018), arXiv:1811.12195 [quant-ph].
 - [15] R. T. Thew, A. Acín, H. Zbinden, and N. Gisin, “Bell-type test of energy-time entangled qutrits,” *Phys. Rev. Lett.* **93**, 010503 (2004).
 - [16] J. Brendel, N. Gisin, W. Tittel, and H. Zbinden, “Pulsed energy-time entangled twin-photon source for quantum communication,” *Phys. Rev. Lett.* **82**, 2594–2597 (1999).
 - [17] Anand Kumar Jha, Mehul Malik, and Robert W. Boyd, “Exploring energy-time entanglement using geometric phase,” *Phys. Rev. Lett.* **101**, 180405 (2008).
 - [18] Jean-Philippe W. MacLean, John M. Donohue, and Kevin J. Resch, “Direct characterization of ultrafast energy-time entangled photon pairs,” *Phys. Rev. Lett.* **120**, 053601 (2018).
 - [19] Alipasha Vaziri, Gregor Weihs, and Anton Zeilinger, “Experimental two-photon, three-dimensional entanglement for quantum communication,” *Phys. Rev. Lett.* **89**, 240401 (2002).
 - [20] Jonathan Leach, Barry Jack, Jacqui Romero, Anand K Jha, Alison M Yao, S. Franke-Arnold, David G Ireland, Robert W Boyd, Stephen M Barnett, and Miles J Padgett, “Quantum Correlations in Optical Angle-Orbital Angular Momentum Variables,” *Science* **329**, 662–665 (2010).
 - [21] Mario Krenn, Mehul Malik, Manuel Erhard, and Anton Zeilinger, “Orbital angular momentum of photons and the entanglement of laguerre-gaussian modes,” *Philosophical Transactions of the Royal Society A: Mathematical, Physical and Engineering Sciences* **375** (2017).
 - [22] Manuel Erhard, Robert Fickler, Mario Krenn, and Anton Zeilinger, “Twisted photons: New quantum perspectives in high dimensions,” *Light: Science and Applications* **7**, 17146 (2018).
 - [23] John C. Howell, Ryan S. Bennink, Sean J. Bentley, and R. W. Boyd, “Realization of the einstein-podolsky-rosen paradox using momentum- and position-entangled photons from spontaneous parametric down conversion,” *Phys. Rev. Lett.* **92**, 210403 (2004).
 - [24] Christoph Schaeff, Robert Polster, Marcus Huber, Sven Ramelow, and Anton Zeilinger, “Experimental access to higher-dimensional entangled quantum systems using integrated optics,” *Optica* **2**, 523–529 (2015).
 - [25] Jianwei Wang, Stefano Paesani, Yunhong Ding, Raffaele Santagati, Paul Skrzypczyk, Alexia Salavrakos, Jordi Tura, Remigiusz Augusiak, Laura Mančinska, Davide Bacco, Damien Bonneau, Joshua W. Silverstone, Qihuang Gong, Antonio Acín, Karsten Rottwitt, Leif K. Oxenløwe, Jeremy L. O’Brien, Anthony Laing, and Mark G. Thompson, “Multidimensional quantum entanglement with large-scale integrated optics,” *Science* **360**, 285–291 (2018).
 - [26] Tristan Kraft, Christina Ritz, Nicolas Brunner, Marcus Huber, and Otfried Gühne, “Characterizing genuine multilevel entanglement,” *Phys. Rev. Lett.* **120**, 060502 (2018).
 - [27] Marcus Huber and Marcin Pawłowski, “Weak randomness in device-independent quantum key distribution and the advantage of using high-dimensional entanglement,” *Phys. Rev. A* **88**, 032309 (2013).
 - [28] Helle Bechmann-Pasquinucci and Asher Peres, “Quantum cryptography with 3-state systems,” *Phys. Rev. Lett.* **85**, 3313–3316 (2000).
 - [29] H. Bechmann-Pasquinucci and W. Tittel, “Quantum cryptography using larger alphabets,” *Phys. Rev. A* **61**, 062308 (2000).
 - [30] Nicolas J. Cerf, Mohamed Bourennane, Anders Karlsson, and Nicolas Gisin, “Security of quantum key distribution using d -level systems,” *Phys. Rev. Lett.* **88**, 127902 (2002).
 - [31] Georgios M. Nikolopoulos and Gernot Alber, “Security bound of two-basis quantum-key-distribution protocols using qudits,” *Phys. Rev. A* **72**, 032320 (2005).
 - [32] Lana Sheridan and Valerio Scarani, “Security proof for quantum key distribution using qudit systems,” *Phys. Rev. A* **82**, 030301 (2010).
 - [33] Irfan Ali-Khan, Curtis J. Broadbent, and John C. Howell, “Large-alphabet quantum key distribution using energy-time entangled bipartite states,” *Phys. Rev. Lett.* **98**, 060503 (2007).
 - [34] Zheshen Zhang, Maria Tengner, Tian Zhong, Franco N. C. Wong, and Jeffrey H. Shapiro, “Entanglement’s benefit survives an entanglement-breaking channel,” *Phys. Rev. Lett.* **111**, 010501 (2013).
 - [35] Tian Zhong, Hongchao Zhou, Robert D Horansky, Catherine Lee, Varun B Verma, Adriana E Lita, Alessandro Restelli, Joshua C Bienfang, Richard P Mirin, Thomas Gerrits, Sae Woo Nam, Francesco Marsili, Matthew D Shaw, Zheshen Zhang, Ligong Wang, Dirk Englund, Gregory W Wornell, Jeffrey H Shapiro, and Franco N C Wong, “Photon-efficient quantum key distribution using time-energy entanglement with high-dimensional encoding,” *New Journal of Physics* **17**, 022002 (2015).
 - [36] Alicia Sit, Frédéric Bouchard, Robert Fickler, Jérémy Gagnon-Bischoff, Hugo Larocque, Khabat Heshami, Dominique Elser, Christian Peuntinger, Kevin Günthner, Bettina Heim, Christoph Marquardt, Gerd Leuchs, Robert W. Boyd, and Ebrahim Karimi, “High-dimensional intracity quantum cryptography with structured photons,” *Optica* **4**, 1006–1010 (2017).
 - [37] Frédéric Bouchard, Khabat Heshami, Duncan England, Robert Fickler, Robert W. Boyd, Berthold-Georg Englert, Luis L. Sánchez-Soto, and Ebrahim Karimi, “Experimental investigation of high-dimensional quantum key distribution protocols with twisted photons,” *Quantum* **2**, 111 (2018).
 - [38] Feng Zhu, Max Tyler, Natalia Herrera Valencia, Mehul Malik, and Jonathan Leach, “Are high-dimensional entangled states robust to noise?” (2019), arXiv:1908.08943 [quant-ph].
 - [39] Daniel Collins, Nicolas Gisin, Noah Linden, Serge Massar, and Sandu Popescu, “Bell inequalities for arbitrarily high-dimensional systems,” *Phys. Rev. Lett.* **88**, 040404 (2002).

- [40] Asher Peres, “Separability criterion for density matrices,” *Phys. Rev. Lett.* **77**, 1413–1415 (1996).
- [41] Michał Horodecki, Paweł Horodecki, and Ryszard Horodecki, “Separability of mixed states: necessary and sufficient conditions,” *Physics Letters A* **223**, 1 – 8 (1996).
- [42] Guifré Vidal and Rolf Tarrach, “Robustness of entanglement,” *Phys. Rev. A* **59**, 141–155 (1999).
- [43] Michał Horodecki and Paweł Horodecki, “Reduction criterion of separability and limits for a class of distillation protocols,” *Physical Review A* **59**, 4206–4216 (1999).
- [44] Ludovico Lami and Marcus Huber, “Bipartite depolarizing maps,” *Journal of Mathematical Physics* **57** (2016).
- [45] Jessica Bavaresco, Natalia Herrera Valencia, Claude Klöckl, Matej Pivoluska, Paul Erker, Nicolai Friis, Mehul Malik, and Marcus Huber, “Measurements in two bases are sufficient for certifying high-dimensional entanglement,” *Nature Physics* **14**, 1032–1037 (2018).
- [46] Thomas Brougham and Stephen M. Barnett, “Information communicated by entangled photon pairs,” *Phys. Rev. A* **85**, 032322 (2012).
- [47] See Supplemental Material for the derivation of an entanglement witness, the definition of the Noise Fraction NF , the discretization of the time-domain, details on the error analysis and correlation measurements of the OAM experiment.
- [48] J. D. Franson, “Bell inequality for position and time,” *Phys. Rev. Lett.* **62**, 2205–2208 (1989).
- [49] D. V. Strekalov, T. B. Pittman, A. V. Sergienko, Y. H. Shih, and P. G. Kwiat, “Postselection-free energy-time entanglement,” *Phys. Rev. A* **54**, R1–R4 (1996).
- [50] Paul G. Kwiat, “Hyper-entangled states,” *Journal of Modern Optics* **44**, 2173–2184 (1997).
- [51] Julio T. Barreiro, Nathan K. Langford, Nicholas A. Peters, and Paul G. Kwiat, “Generation of hyperentangled photon pairs,” *Phys. Rev. Lett.* **95**, 260501 (2005).
- [52] Taehyun Kim, Marco Fiorentino, and Franco N. C. Wong, “Phase-stable source of polarization-entangled photons using a polarization sagnac interferometer,” *Phys. Rev. A* **73**, 012316 (2006).
- [53] Alessandro Fedrizzi, Thomas Herbst, Andreas Poppe, Thomas Jennewein, and Anton Zeilinger, “A wavelength-tunable fiber-coupled source of narrow-band entangled photons,” *Optics Express* **15**, 15377 (2007).
- [54] Frédéric Bouchard, Natalia Herrera Valencia, Florian Brandt, Robert Fickler, Marcus Huber, and Mehul Malik, “Measuring azimuthal and radial modes of photons,” *Optics Express* **26**, 31925 (2018).
- [55] Thomas Durt, Berthold-Georg Englert, Ingemar Bengtsson, and Karol Życzkowski, “On mutually unbiased bases,” *International journal of quantum information* **8**, 535–640 (2010).
- [56] Christoph Spengler, Marcus Huber, Stephen Brierley, Theodor Adaktylos, and Beatrix C. Hiesmayr, “Entanglement detection via mutually unbiased bases,” *Phys. Rev. A* **86**, 022311 (2012).
- [57] Jiří Svozilík, Jan Peřina Jr, and Juan P Torres, “High spatial entanglement via chirped quasi-phase-matched optical parametric down-conversion,” *Physical Review A* **86**, 052318 (2012).
- [58] Matthew P Peloso, Ilja Gerhardt, Caleb Ho, Antía Lamas-Linares, and Christian Kurtsiefer, “Daylight operation of a free space, entanglement-based quantum key distribution system,” *New Journal of Physics* **11**, 045007 (2009).
- [59] Sheng-Kai Liao, Hai-Lin Yong, Chang Liu, Guo-Liang Shentu, Dong-Dong Li, Jin Lin, Hui Dai, Shuang-Qiang Zhao, Bo Li, Jian-Yu Guan, Wei Chen, Yun-Hong Gong, Yang Li, Ze-Hong Lin, Ge-Sheng Pan, Jason S. Pelc, M. M. Fejer, Wen-Zhuo Zhang, Wei-Yue Liu, Juan Yin, Ji-Gang Ren, Xiang-Bin Wang, Qiang Zhang, Cheng-Zhi Peng, and Jian-Wei Pan, “Long-distance free-space quantum key distribution in daylight towards inter-satellite communication,” *Nature Photonics* **11**, 509–513 (2017).
- [60] Mario Krenn, Johannes Handsteiner, Matthias Fink, Robert Fickler, Rupert Ursin, Mehul Malik, and Anton Zeilinger, “Twisted light transmission over 143 km,” *Proceedings of the National Academy of Sciences* **113**, 13648–13653 (2016).
- [61] Mohammad Mirhosseini, Mehul Malik, Zhimin Shi, and Robert W. Boyd, “Efficient separation of the orbital angular momentum eigenstates of light,” *Nature Communications* **4**, 2781 (2013).
- [62] Stefan Bäuml, Andreas Winter, and Dong Yang, “Every entangled state provides an advantage in classical communication,” *Journal of Mathematical Physics* **60**, 072201 (2019).
- [63] Marco Piani and John Watrous, “All entangled states are useful for channel discrimination,” *Phys. Rev. Lett.* **102**, 250501 (2009).
- [64] Marcus Huber and Julio I. de Vicente, “Structure of multidimensional entanglement in multipartite systems,” *Phys. Rev. Lett.* **110**, 030501 (2013).
- [65] Alois Mair, Alipasha Vaziri, Gregor Weihs, and Anton Zeilinger, “Entanglement of the orbital angular momentum states of photons,” *Nature* **412**, 313 (2001).
- [66] Marcus Huber, Martí Perarnau-Llobet, and Julio I. de Vicente, “Entropy vector formalism and the structure of multidimensional entanglement in multipartite systems,” *Phys. Rev. A* **88**, 042328 (2013).

SUPPLEMENTARY INFORMATION

1. Pathway I - Entanglement witness derivation

In order to certify entanglement in the energy-time experiment (Pathway I), we appealed to the entropy vector method, first introduced in [64] and elucidated in [66], which was used to investigate the structure of multipartite entanglement. Consider the pure state ρ consisting of n parties. Let r denote a particular subset of parties, i.e. a subset of $\{1, 2, \dots, n\}$, and let \bar{r} denote the complement. The set \mathcal{R} denotes a further subset of r . For pure states ρ , the components of the linear entropy vector \vec{S}_L are given by

$$S_L^j(\rho) \geq -\log_2 \left(1 - \frac{W_j(\rho, C, \mathcal{R})^2}{2} \right) \quad (8)$$

where the witness for the j -th component of the vector is given by

$$W_j(\rho, C, \mathcal{R}) := \frac{1}{|\sqrt{C}|} \sum_{\eta, \eta' \in C} \left(\langle \eta | \rho | \eta' \rangle - \min_{\{r_m\} \in \mathcal{R}} \sum_{m=1}^j \sqrt{\langle \eta_{r_m} | \rho | \eta_{r_m} \rangle \langle \eta'_{r_m} | \rho | \eta'_{r_m} \rangle} \right). \quad (9)$$

Here η is a multi-index (e.g. the triple 110 for a tripartite qubit state), and the pair $(\eta_{r_m}, \eta'_{r_m})$ is the pair (η, η') with the indicies of the r_m subset of parties exchanged. C is a set of indices over which the witness runs, and can be chosen as desired. Intuitively, this witness sums particular off-diagonal terms from the density matrix, and penalises those on the diagonal. As was shown in [64, 66], if all entries of \vec{S}_L are non-zero then the n -partite state cannot be written as a convex combination of separable states

$$\rho \neq \sum_i p_i \rho_{r_i} \otimes \rho_{\bar{r}_i} \quad (10)$$

i.e. the state has no separable decomposition, which implies that it is entangled. Since we are working to verify the entanglement of a bipartite state ρ_{AB} , this trivially selects the set $\mathcal{R} = \{A\}^1$ such that $j = 1$ in Eq. (9) and the sum and minimisation vanish. Thus, \vec{S}_L has one component, and if it is non-zero then

$$\rho_{AB} \neq \sum_i p_i \rho_{A_i} \otimes \rho_{B_i} \quad (11)$$

and entanglement is certified. From Eq. (8) it can be seen that each witness W_j provides a lower bound on each component S_L^j of the entropy vector; thus a necessary condition for ρ_{AB} to be entangled is that $W_1(\rho_{AB}, C, \{A\}) > 0$.

In principle, in order to get the best witness out of Eq. (9) one may play with the set C in order to maximise the expression. In this work we do not perform such an optimisation and simply take the set to be $C = \{((i, i), (i+1, i+1))\}_1^{d-1}$, since we anticipate the produced state to be close to $|\Phi^+\rangle \langle \Phi^+| = \sum_{ij} \frac{1}{d} |ii\rangle \langle jj|$. This move means that we present a lower bound on the witness in Eq. (12) which, as we shall show, is sufficient to verify entanglement anyway. With these definitions in place the witness becomes

$$W_1(\rho) := \frac{1}{\sqrt{d-1-f}} \left(\sum_i^{d-f} \langle ii | \rho | i+1, i+1 \rangle - \sqrt{\langle i, i+1 | \rho | i, i+1 \rangle \langle i+1, i | \rho | i+1, i \rangle} \right), \quad (12)$$

where we have dropped the subscript AB for convenience. From this expression, it is clear that the maximum value of the witness is achieved on the maximally entangled state $W_1(|\Phi^+\rangle \langle \Phi^+|) = \frac{d-1}{d\sqrt{d-1}}$. Moreover, it is clear that if we take $C = \{((i, i), (i+f, i+f))\}_1^{d-1}$ for integer f , then

$$W_1(\rho) := \frac{1}{\sqrt{d-1}} \left(\sum_i^{d-1} \langle ii | \rho | i+f, i+f \rangle - \sqrt{\langle i, i+f | \rho | i, i+f \rangle \langle i+f, i | \rho | i+f, i \rangle} \right), \quad (13)$$

is also a valid entanglement witness. Due to the particulars of the experimental setup, we will work with the above expression. In order to compute the value of the witness on the state that is produced by experiment, we must reconstruct the density matrix elements of ρ from the count matrices. In short, the first term in Eq. (13) is not a number we have direct access to, and thus it must be computed (in fact bounded) from the data; on the other hand, the term in the square root is measured and can be extracted directly from the experimental data.

The time-bin entanglement experiment provides count matrices for detection clicks produced by making one of two

¹ Or equivalently $\{B\}$ under symmetry.

measurements on Alice and Bob's photons. These are either the 'computational basis', or the 'Franson basis', alluded to in the main text, which, for convenience, we refer to from here on as the 'horizontal' (HV) and 'diagonal' (DA) bases. The same local measurement is always performed on each side, i.e., either $M_A^{\text{DA}} \otimes M_B^{\text{DA}}$ or $M_A^{\text{HV}} \otimes M_B^{\text{HV}}$, is measured. The polarisation degree of freedom of the photon pairs in the post-selection free Franson interferometer is used as a proxy for detecting the time-bin that Alice and Bob's photons landed in. Thus, a measurement in either of these bases corresponds to one of 4 possible events, namely a click in one of the detector pairs $\{A0B0, A0B1, A1B0, A1B1\}$. The task is to compute the entanglement witness on the energy-time entangled state $W_1(\rho_{ET})$. For polarisation measurements in the HV basis, the full polarisation and time-bin entangled state $\rho_{P,ET}$ is related to the experimental count matrices in the following way:

$$\begin{aligned} \langle HH|\langle ij|\rho_{P,ET}|ij\rangle|HH\rangle &= \frac{\langle i|HV_{A0B0}|j\rangle}{N_1} \\ \langle HV|\langle ij|\rho_{P,ET}|ij\rangle|HV\rangle &= \frac{\langle i|HV_{A0B1}|j+f\rangle}{N_1} \\ \langle VH|\langle ij|\rho_{P,ET}|ij\rangle|VH\rangle &= \frac{\langle i+f|HV_{A1B0}|j\rangle}{N_1} \\ \langle VV|\langle ij|\rho_{P,ET}|ij\rangle|VV\rangle &= \frac{\langle i+f|HV_{A1B1}|j+f\rangle}{N_1} \end{aligned} \quad (14)$$

where $N_1 = \sum_{k,l=0}^1 \sum_{i=1-k}^{d-1-k} \sum_{j=1-l}^{d-1-l} \langle i|HV_{AkBl}|j\rangle$ is the normalisation over all counts and f is a known delay due to the interferometer imbalance². From this, we are able to determine the diagonal elements of the energy-time matrix ρ_{ET} by eliminating (i.e. summing over) the polarisation,

$$\langle ij|\rho_{ET}|ij\rangle = \frac{\sum_{k,l=0}^1 \langle i+f, k|HV_{AkBl}|j+f, l\rangle}{N_1}. \quad (15)$$

To reconstruct the density matrices from the count matrices pertaining to measurements in the DA basis one has to do a little more work. The DA basis performs measurements due to the non-orthogonality of projections onto neighbouring bin pairs. We proceed by showing the relation for the first two count matrices,

$$\frac{1}{4} \left(\langle Hi| + \langle Vi+f| \right)_A \left(\langle Hj| + \langle Vj+f| \right)_B \rho_{P,ET} \left(|Hi\rangle + |Vi+f\rangle \right)_A \left(|Hj\rangle + |Vj+f\rangle \right)_B = \frac{\langle i|DA_{A0B0}|j\rangle}{N_2} \quad (16)$$

$$\frac{1}{4} \left(\langle Hi| - \langle Vi+f| \right)_A \left(\langle Hj| - \langle Vj+f| \right)_B \rho_{P,ET} \left(|Hi\rangle - |Vi+f\rangle \right)_A \left(|Hj\rangle - |Vj+f\rangle \right)_B = \frac{\langle i|DA_{A1B1}|j\rangle}{N_2} \quad (17)$$

Let $p_+ = \langle HH|\rho_P|HH\rangle + \langle VV|\rho_P|VV\rangle$ and $p_- = \langle HV|\rho_P|HV\rangle + \langle VH|\rho_P|VH\rangle$. We take $i = j$, and assume that $\rho_{P,ET} = \rho_P \otimes \rho_{ET}$. This being justified by the fact that across the partition between the 2-dimensional polarization and d -dimensional time-bin states on Alice and Bob, the maximum Schmidt number is 2. Moreover, since we expect the time-bin state to be close to maximally entangled, by monogamy we should expect close to zero entanglement across the partition with polarization. With this in place, we have that the sum of these terms is

$$\begin{aligned} & \sum_{i=0}^d \frac{1}{2} (p_+ \langle ii|\rho_{ET}|ii\rangle + p_- \langle i, i+f|\rho_{ET}|ii+f\rangle + p_- \langle i+f, i|\rho_{ET}|i+f, i\rangle + p_+ \langle i+f, i+f|\rho_{ET}|i+f, i+f\rangle) \\ & + \Re e[\langle HH|\rho_P|VV\rangle \langle ii|\rho_{ET}|i+f, i+f\rangle] + \Re e[\langle HV|\rho_P|VH\rangle \langle i, i+f|\rho_{ET}|i+f, i\rangle] + c \end{aligned} \quad (18)$$

where $N_2 = N_1 \eta_{HWP}^2$ and η_{HWP} is the efficiency of the half-wave-plate used for selecting the basis. Note that the constant c enters due to boundary effects where terms at the beginning and end of the summation do not cancel due to the shift f . The other two count matrices are calculated to be

$$\frac{1}{4} \left(\langle Hi| + \langle Vi+f| \right)_A \left(\langle Hj| - \langle Vj+f| \right)_B \rho_{P,ET} \left(|Hi\rangle + |Vi+f\rangle \right)_A \left(|Hj\rangle - |Vj+f\rangle \right)_B = \frac{\langle i|DA_{A0B1}|j\rangle}{N_2} \quad (19)$$

$$\frac{1}{4} \left(\langle Hi| - \langle Vi+f| \right)_A \left(\langle Hj| + \langle Vj+f| \right)_B \rho_{P,ET} \left(|Hi\rangle - |Vi+f\rangle \right)_A \left(|Hj\rangle + |Vj+f\rangle \right)_B = \frac{\langle i|DA_{A1B0}|j\rangle}{N_2}. \quad (20)$$

² Note that $f = f(d)$ depends on the dimension that the frame F is divided into, and the experimental parameters are always chosen such that f is an integer.

The sum of which is

$$\sum_{i=0}^d \frac{1}{2} (p_+ \langle ii | \rho_{ET} | ii \rangle + p_- \langle i, i+f | \rho_{ET} | i, i+f \rangle + p_- \langle i+f, i | \rho_{ET} | i+f, i \rangle + p_+ \langle i+f, i+f | \rho_{ET} | i+f, i+f \rangle) - \Re e[\langle HH | \rho_P | VV \rangle \langle ii | \rho_{ET} | i+f, i+f \rangle] - \Re e[\langle HV | \rho_P | VH \rangle \langle i, i+f | \rho_{ET} | i+f, i \rangle] + c. \quad (21)$$

Taking the following, particular, linear combination of these matrices

$$\sum_{i=0}^{d-f} \frac{\langle i | DA_{A0B0} | i \rangle}{N_2} + \frac{\langle i | DA_{A1B1} | i \rangle}{N_2} - \frac{\langle i | DA_{A0B1} | i \rangle}{N_2} - \frac{\langle i | DA_{A1B0} | i \rangle}{N_2} = \sum_{i=0}^{d-f} 2 \Re e[\langle HH | \rho_P | VV \rangle \langle ii | \rho_{ET} | i+f, i+f \rangle] + 2 \Re e[\langle HH | \rho_P | VV \rangle \langle i, i+f | \rho_{ET} | i+f, i \rangle] \quad (22)$$

we are able to bound the first term appearing in the witness in Eq. (12)

$$\sum_{i=0}^{d-f} |\langle ii | \rho_{ET} | i+f, i+f \rangle| \geq \sum_{i=0}^{d-3-f} \left(\frac{\langle i | DA_{A0B0} | i \rangle}{N_2} + \frac{\langle i | DA_{A1B1} | i \rangle}{N_2} - \frac{\langle i | DA_{A0B1} | i \rangle}{N_2} - \frac{\langle i | DA_{A1B0} | i \rangle}{N_2} - 2 \sqrt{\langle HV | \rho_P | HV \rangle \langle VH | \rho_P | VH \rangle} \sqrt{\langle i+f, i | \rho_{ET} | i+f, i \rangle \langle i, i+f | \rho_{ET} | i, i+f \rangle} \right) \quad (23)$$

where we used $\langle HH | \rho_P | VV \rangle \leq \frac{1}{2}$, $|z| \geq \Re e[z]$, and $|\langle ij | \rho | kl \rangle| \leq \sqrt{\langle ij | \rho | ij \rangle \langle kl | \rho | kl \rangle}$. Assuming the worst case algebraic bound $\sqrt{\langle HV | \rho_P | HV \rangle \langle VH | \rho_P | VH \rangle} \leq \frac{1}{2}$, we have

$$W_1(\rho_{ET}) \geq \frac{1}{\sqrt{d-1}} \sum_{i=0}^{d-3-f} \left(\frac{\langle i | DA_{A0B0} | i \rangle}{N_2} + \frac{\langle i | DA_{A1B1} | i \rangle}{N_2} - \frac{\langle i | DA_{A0B1} | i \rangle}{N_2} - \frac{\langle i | DA_{A1B0} | i \rangle}{N_2} - \sqrt{\langle i+f, i | \rho_{ET} | i+f, i \rangle \langle i, i+f | \rho_{ET} | i, i+f \rangle} \right) \quad (24)$$

Our final step is to substitute the terms under the square root with their definition from Eq. (15) and argue that since we are looking for a positive violation $W_1(\rho_{ET}) > 0$ to witness entanglement, then the pre-factor is irrelevant. The final witness we test on the experimental data is thus

$$W_1(\rho_{ET}) \geq \sum_{i=0}^{d-f} \frac{1}{N_2} \left(\langle i | DA_{A0B0} | i \rangle + \langle i | DA_{A1B1} | i \rangle - \langle i | DA_{A0B1} | i \rangle - \langle i | DA_{A1B0} | i \rangle \right) - 2 \sqrt{\frac{1}{N_1} \sum_{k,l=0}^1 \sum_{m,n=0}^1 \langle i+f, i | HV_{AlBk} | i+f, i \rangle \langle i+f, i+f | HV_{AmBn} | i+f, i+f \rangle}, \quad (25)$$

where f is the adjustment we make to the witness in lieu of the interferometer imbalance. In all, we test four dimensions (i.e. discretisations of the frame), which are summarised below.

TABLE I. Different time-frame discretisations with corresponding f-shifts

Dimension d	Time-bin duration in clock cycles (ns)	f-shift
10	32 (2.62)	1
20	16 (1.31)	2
40	8 (0.66)	4
80	4 (0.33)	8

2. Pathway I and II - Definition of the Noise fraction NF

In the main text we quantify the level of noise via the noise fraction NF , which is defined as the total noise divided by the total signal in our detectors. Here, we elaborate on this quantity and discuss how it is extracted from the measurement data of both experiments. Suppose Alice chooses to measure in the basis α , while Bob chooses to

measure in the basis β . The number of two-photon events with measurement outcome $m \in \{0, 1, \dots, d-1\}$ for Alice and $n \in \{0, 1, \dots, d-1\}$ for Bob in their respective bases is given by $N^{(\alpha, \beta)}(m, n)$. Let us first define the NF used in Pathway I. For this Pathway, we quantify the noise exclusively in the computational, or time of arrival (TOA) basis as

$$NF = \frac{\sum_{m=0}^{d-1} \sum_{\substack{n=0 \\ n \neq m}}^{d-1} N^{(\text{TOA}, \text{TOA})}(m, n)}{\sum_{m=0}^{d-1} \sum_{n=0}^{d-1} N^{(\text{TOA}, \text{TOA})}(m, n)}. \quad (26)$$

In the numerator, all uncorrelated or off-diagonal elements of $N^{(\text{TOA}, \text{TOA})}(m, n)$ are summed, while the denominator is the sum over all two-photon events. Pathway II, on the other hand, harnesses all mutually unbiased bases (MUBs) in each dimension d , which means no basis is distinguished. Hence, we average over the noise fractions of all $d+1$ MUBs, yielding

$$NF = \frac{1}{d+1} \sum_{\alpha=0}^d \left(\frac{\sum_{m=0}^{d-1} \sum_{\substack{n=0 \\ n \neq m}}^{d-1} N^{(\alpha, \alpha)}(m, n)}{\sum_{m=0}^{d-1} \sum_{n=0}^{d-1} N^{(\alpha, \alpha)}(m, n)} \right). \quad (27)$$

3. Pathway I - Discretization and correlation measurements

Pathway I is realized by fine-graining the time of arrival of single photons. To this end, the arrival time is discretized in time-bins of duration t_d , and the time-bin number of a photon detection is recorded. The time-bins are numbered from 1 to d , adding up to a time-frame of duration $F = d \cdot t_d$, which is kept constant at 26.2 ns for our experiment. A fixed time-frame duration ensures that the noise rate per frame is constant irrespective of the dimension. There are two constraints on the time-bin duration: Firstly, t_d must be a multiple of the clock cycle of our time to amplitude converter (82.3 ps), and secondly, the fixed imbalance of the Franson interferometer must be a multiple of t_d (see Fig. 4). These constraints yield time-bin durations and f-shifts listed in Table I.

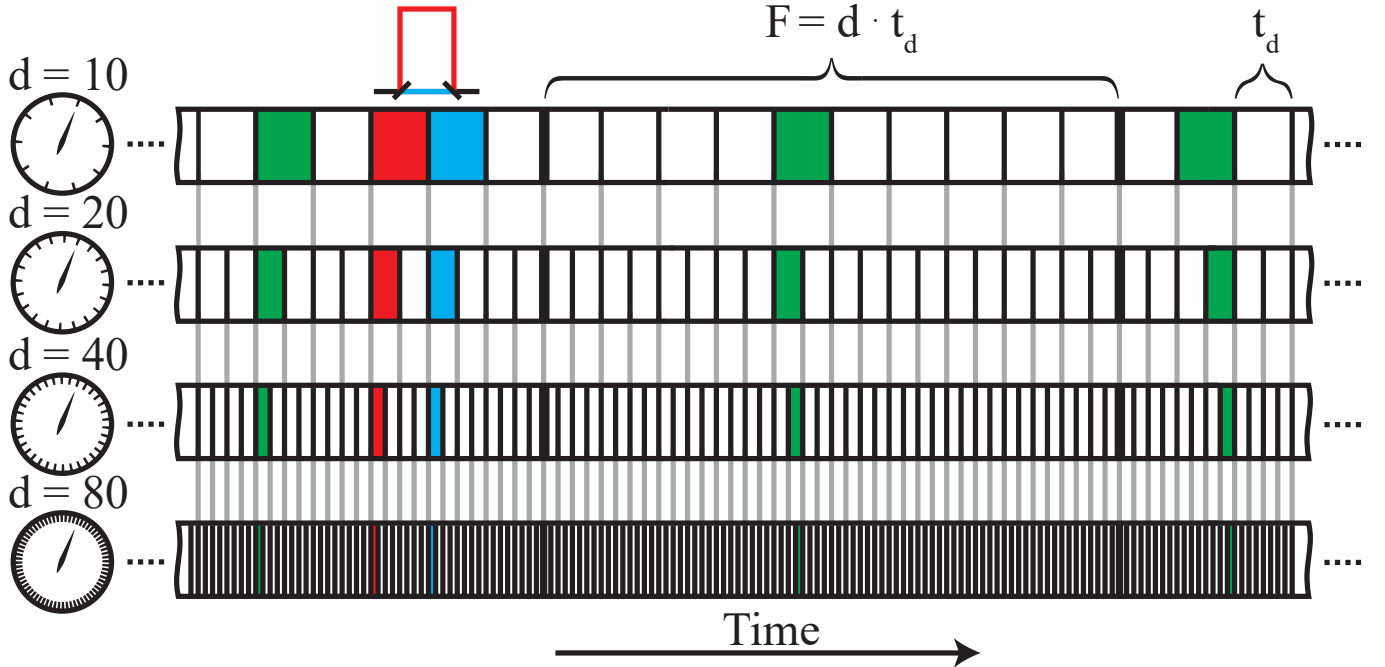


FIG. 4. Discretization of the time domain in time-frames and time-bins of duration t_d with examples of single-photon detection events (in green). The time-frame duration F is kept constant for all dimensions d . Higher dimensions are therefore implemented by decreasing the time-bin duration according to $t_d = \frac{F}{d}$, which leads to Franson interference (in blue-red) between well-defined time-bins irrespective of the dimension.

By applying these 4 discretizations, we now investigate the time-bin correlations between Alice and Bob (Fig. 5). We consider a noise level which is high enough to yield a negative witness for $d = 10/20$ and a positive witness for $d = 40/80$, certifying a separable and an entangled state respectively. The correlated events on the diagonal can be attributed to the maximally energy-time-entangled state emitted by our photon pair source, while the off-diagonal elements arise from our noise source. As a consequence of increasing dimensions, the noise is spread quadratically over the off-diagonal elements, while the correlated events on the diagonal spread linearly with the dimension, which is the key mechanism of Pathway I. However, discretizing to higher dimensions comes at the cost of additional noise induced by measuring close to the time resolution of the single photon detectors. This increasing crosstalk is clearly visible in Fig. 5 (c) and (d).

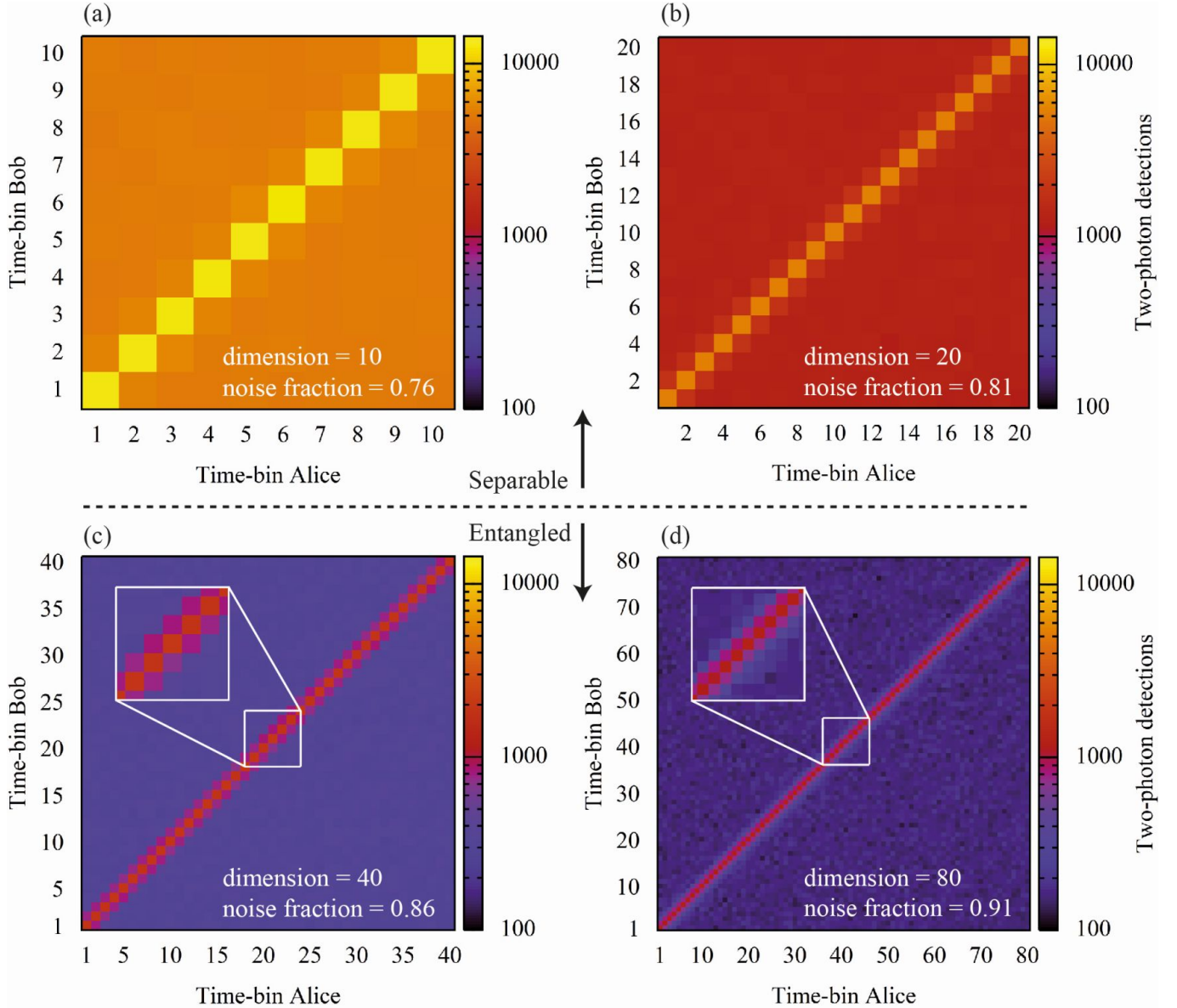


FIG. 5. Two-photon detection events in the time-domain integrated over 4 minutes. The correlated events on the diagonal primarily arise from energy-time entangled photon pairs emitted from a SPDC source, while the off-diagonal elements can be attributed to high levels of external noise. Photon detection-events are discretized in time-bins of dimension $d =$ (a) 10, (b) 20, (c) 40 and (d) 80. The time-frame has a constant duration throughout all dimensions, which leads to a decrease in time-bin duration with increasing d . The plots are generated from detection events between detectors A0 and B1 from a measurement in the Franson basis and at a constant external noise level of ~ 400 kcps per detector. Increasing crosstalk due to timing-jitter leads to an increase in the noise fraction NF in higher dimensions.

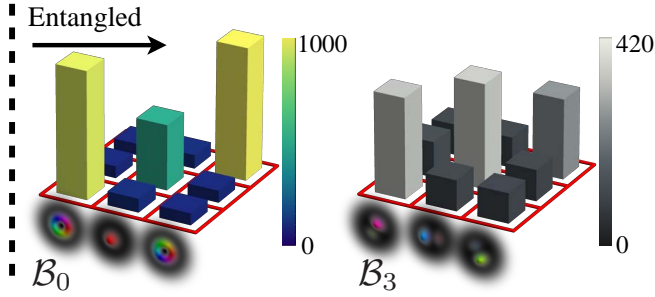
4. Pathway I - Error analysis

In order to produce the error bars for the plot of entanglement detection in Fig. 3 of the main text, we ran a random number generator with Poisson distribution over the experimental data sets. Specifically, we assumed that the photon detections in the count matrices represented the Poissonian mean of the distribution. This comes with the tacit assumption that the probability of photon detection within a certain time interval does not change over the course of the experiment and that the probability of a detection in a particular time interval is independent of the probability of a detection in any other non-overlapping interval. We simulated 150 new data sets, on which we computed an average witness $W(\rho_{\text{sim}})$ and the subsequent standard deviation.

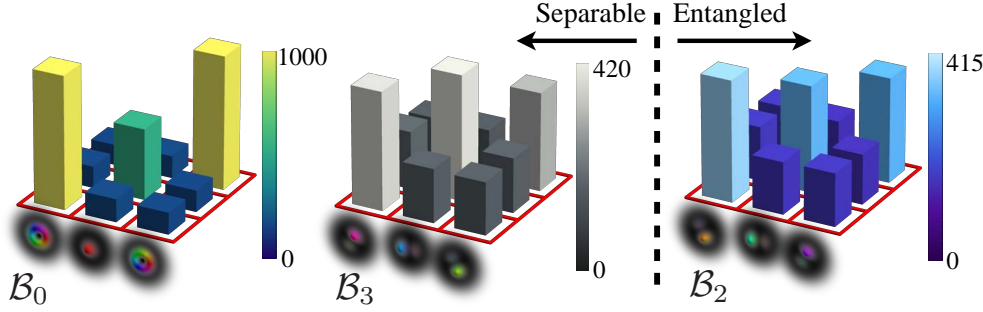
5. Pathway II - Correlation measurements

Here, we present direct correlation measurements for the case of OAM entanglement with $d = 3$. In Pathway II, larger noise fraction can be tolerated by including measurements in additional mutually unbiased bases (MUB). Correlation matrices, given in terms of coincidence counts, are shown for three different noise fractions, see Fig. 6. In Fig. 6(a), we were able to tolerate a noise fraction of 0.36 up to which entanglement can still be certified with measurements in only 2 MUBs. The measurements were done in MUB \mathcal{B}_0 (the OAM computational basis) and MUB \mathcal{B}_3 , where the visibility sum ($\sum V$) is still larger than $4/3$. We recall that the upper bound for separable states is given by $\sum_{j=0}^{k-1} V^{(j,j)} \leq 1 + \frac{k-1}{d}$, where k is the number of MUBs considered. In Fig. 6(b), we considered the measurements in three MUBs, which led to a verification of entanglement up to a noise fraction of 0.45. Here, the measurements in MUBs \mathcal{B}_0 , \mathcal{B}_2 , and \mathcal{B}_3 were taken into account, where the visibility sum ($\sum V$) is still larger than $5/3$. Finally, in Fig. 6(c), we performed measurements in all 4 MUBs to show the largest resilience to noise. For a noise fraction of up to 0.48, we were able to verify entanglement, where the visibility sum ($\sum V$) is still larger than 2.

(a) noise fraction = 0.36



(b) noise fraction = 0.45



(c) noise fraction = 0.48

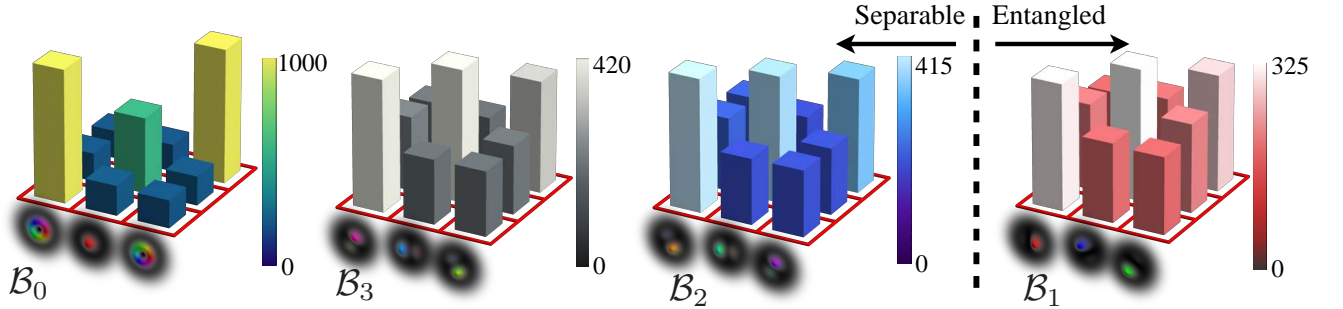


FIG. 6. Detecting three-dimensional OAM entanglement between two photons with increasing noise fraction. Each graph shows the correlation measurements, given in coincidence counts per second, between Alice's (x-axis) and Bob's (y-axis) photon for all modes of a mutually unbiased basis (MUB). For a low noise fraction, the measurements in two MUBs are already enough to verify entanglement as depicted by the threshold (dashed line) on the left side in (a). When the noise fraction is increased the threshold moves to the right, which means that more MUBs need to be measured to still verify entanglement, as can be seen in (b) and (c). Only high-dimensionally entangled states allow to measure in more than 3 MUBs, which is the fundamental idea behind Pathway II to noise resilience.